Materials Research Proceedings 44 (2024) 411-424 https://doi.org/10.21741/9781644903254-45

Investigation of mesoscale deformation and damage behaviour in high-carbon bearing steel via multiscale simulations and experiments

WANG Huiling[1,a], QIAN Dongsheng[1,b*], WANG Feng[1,c], and HUA Lin[1,d]

[1]West Courtyard, Mafanshan Campus, No. 122, Luoshi Road, Hongshan District, Wuhan City, Hubei Province, China

[a]wanghlwhut@163.com, [b]qiands@whut.edu.cn,
[c]wangfengwhut@163.com, [d]hualin@whut.edu.cn.com

Keywords: High-Carbon Steel, In Situ SEM, Digital Image Correlation, Multiscale Simulations, Damage and Fracture, Representative Volume Element, Molecular Dynamics

Abstract. High-carbon steel is susceptible to micro-defects owing to the heterogeneous microstructures during forming, which seriously deteriorates the fatigue life. However, the investigation of the damage behavior during cold deformation remains largely undisclosed in these steels, which hinders further control of the microstructure and forming process. The current work investigates the deformation and damage characteristics of high-carbon steel composed of soft ferrite and hard cementite particles. A methodology coupled with multiscale simulations and experiments is applied to analyze large plastic deformation and damage characteristics. The simulation utilizes nanoscale molecular dynamics simulation to obtain matrix-particle interface strength properties. The Rice-Tracey fracture model and Weibull distribution capture experimental fracture characteristics of matrix and particles. The above failure criteria are incorporated within a real microstructure-based representative volume element (RVE) to conduct the mesoscale deformation and damage process in the spheroidized ferrite-cementite steel. Additionally, in-situ SEM uniaxial tensile tests are carried out to assess the damage mechanism and validity of the mesoscale simulation. The numerical simulation exhibits a well coincidence with the experimental trends in damage evolution of the individual particles, matrix, and matrix/particle interfaces. It is also observed that damage is a function of inherent particle properties, particle morphological features, and matrix strain localization characteristics. Larger-size and long-striped particle undergoes fracture at an earlier stage. Consequently, the incompatibility and stress concentration between matrix and particles affect the strain localization characteristics. As a result, higher stresses inside strain localization bands results in the increase of void damage initiation and growth along the interfaces. Overall, the way of matrix/particle decohesion should be marginally higher compared to particle fracture, which primarily dominates the final fracture of the high-carbon bearing steel.

Introduction

High-carbon bearing steels have been widely used in the aerospace, precision machine tool, and automotive industries because of its the relatively high machinability, good ductility, and excellent surface finish [1-3]. However, as a dual-phase polycrystalline alloy, micro-defects are highly susceptible to be produced in these steels owing to the mismatched deformation between the ferrite and cementite during cold-forming [4, 5]. These defects act as crack sources and reduce the impact toughness [6] and fatigue life [7]. This phenomenon is mainly influenced by the interleaving of length-scales caused by the deformation geometry, loading conditions and/or heterogeneous microstructure of the material. From the early studies [8-12], clearly the microstructural factors such as grain size, particle size, distribution, mechanical properties of the constituent phases, should be considered in analysis of deformation and fracture behavior. This complex

microstructure with different phases produces a highly non-uniform stress and strain distribution in the localized microstructure. However, the complexity of the microstructure makes it difficult to capture this strain distribution and damage response. There have been some studies on the damage mechanism of dual-phase steels numerically and experimentally, but less research has been done on the damage and strain distribution phenomena of this microstructure of cementite steel. Therefore, it is necessary to study the local deformation and damage mechanism of these steels in detail, as well as the correlation between them and the microstructure parameters.

In recent years, numerical simulation has been the most popular method to investigate the ductile damage and fracture behavior of metals, such as macroscale finite element (FE) simulation [13-15], nanoscale molecular dynamics (MD) [16, 17] simulation, and mesoscale representative volume element (RVE) methods [18-22]. From a macroscale level, the information about the failure properties of the components can be predicted through macroscale FE simulations, such as the stress and strain evolution of the components during the complex molding and manufacturing process. From the crystal and phase level, the correlation between the mesoscopic mechanical properties in the material with the microstructural characteristics can be accessed from RVE simulations. From the atomic level, the intrinsic properties can be described by MD simulation. Based on these numerical calculations, the damage and fracture mechanisms can be detected that have not yet been revealed only through experiments. In this way, a variety of damage models can be developed that are suitable for application in different materials and forming processes. Thus, the combination of micro-, macro-, and nanoscale simulation greatly enriches the understanding of damage and fracture processes in metals and other engineering materials.

In addition, the latest advancement of in situ experiment coupled with micro Digital Image Correlation (μDIC) has been also an effective method for observing the damage mechanism and non-uniform strain distribution in multiphase microstructure. For instance, [23] studied the neighborhood effects on micromechanical behaviors of multi-phase TRIP steel by employing in situ SEM/EBSD and in situ synchrotron X-ray diffraction tensile tests. [24] analyzed the evolution of the whole damage process of SiCp/Al composites through in situ tensile testing. [25] provided a unique set of data including twin/detwin characteristics and twin area fraction of Mg alloys by the in situ SEM-DIC method. [26] investigated the strain localization in commercially pure titanium under uniaxial tension by means of in situ digital image correlation (DIC) at different length scales. [19] observed the dominant damage nucleation mode changed from ferrite grain boundary (F/F) decohesion to ferrite/martensite interface (F/M) decohesion and finally to martensite cracking by in-situ tensile testing in a SEM. The microstructure of high-carbon bearing steels is a mixture of a mechanically soft phase (ferrite matrix) and hard phases (cementite particles), and as a result of their distinct deformation behaviors, the amount of plastic strain partitioned into these phases varies significantly [4]. On top of these points about strain partitioning, there is also microstructural strain path development that needs to be taken into account.

In this work, the multiscale simulations and the in-situ SEM-based μDIC were combined to investigate the damage evolution and failure behavior of high-carbon bearing steel under the uniaxial tensile loading. First, the microstructure characteristics and damage mechanism of the as-received material was characterized by the in-situ SEM-based μDIC. Second, macroscale tensile model was conducted based on the experimental sample, and the GTN plasticity model was used in the model. Third, a microstructure-based RVE from the in-situ SEM image was reconstructed to analyze the micromechanical behavior, and estimate the failure model parameters of two phases. In particular, the zero-thickness cohesive elements were inserted at ferrite/carbide interfaces. Thereafter, the isotropic elastoplastic model, damage criterion, and CZM were assigned to the ferrite, cementite, and interface elements, whereas the elastic property was considered for the carbides. Fourth, the nanoscale MD model under different angle loading was performed by using

the LAMMPS software. For the purpose of identifying the model parameters, the RSM method was applied to evaluate the GTN parameters, and then MD simulations were used to obtain the CZM parameters. The μDIC analysis from in-situ results was used to estimate the damage model parameters of two phases. Finally, the validity of the model was evaluated by comparing with the in-situ tensile results. Specifically, the ductile fracture, micromechanical behavior, damage evolution of the high-carbon bearing steel were explored.

Methodology

Experiments. The as-received material used in this study was the annealed 1.0C-1.5Cr steel bar with a size of Ø50 × 110 mm. The chemical composition is listed in Table 1. The initial microstructure was characterized by a Quanta FEG 450 Scanning Electron Microscope (SEM) and a JEOL-2100F high resolution transmission electron microscopy (HRTEM). The specimen for SEM observation was mechanically polished and then etched in an alcohol solution containing 4% nitric acid (volume fraction) for 30 s. The specimen used for HRTEM experiment was prepared by mechanical polishing into the disk with the thickness of 50 μm, and then thinned by twin-jet electrolytic polishing apparatus. To determine the OR and coherency of ferrite/cementite interface, electron diffraction pattern and HRTEM images of the selected region were evaluated by means of Digital Micrograph software tool and fast Fourier transformation (FFT), respectively.

Table 1. Chemical composition of the as-received material.

Element	C	Cr	Si	Mn	Mo	Ni	P	S	Cu	Fe
Wt [%]	0.967	1.38	0.30	0.23	0.02	0.07	0.02	<0.023	0.05	Bal.

In-situ SEM tensile tests were conducted to observe the damage evolution and strain field at room temperature using a Gemini 300 SEM equipment. The dimensions and geometry of the tested specimens are shown in Fig. 1(a). Before the tensile tests, the specimens were mechanically polished, followed by ultrasonic cleaning with acetone, and electropolishing in an alcohol solution containing 4% nitric acid. During the tensile test, the specimen was deformed at with a velocity of 0.033 mm/min, and microstructures were captured by the repeated interruptions at the local strains of 2%, 5%, 10%, 15% and 20%. Fig. 1(b) shows the force-displacement curve for in situ tensile test. In addition, evolution of the equivalent plastic strain field (PEEQ) from undeformed to deformed in-situ SEM images was captured based on μDIC technology.

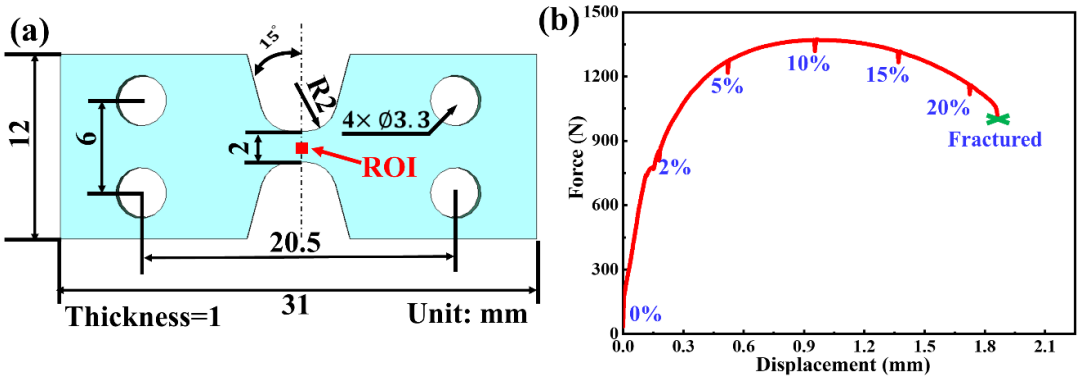

Fig. 1. (a) Dimensions of the specimen for in situ tensile tests. (b) Force-displacement curve.

The uniaxial tensile tests were conducted at room temperature on an AG-IC universal material testing machine. Standard tensile specimens were machined from adjacent locations on the as-

received bar to ensure similarly of the microstructure. Fig. 2 shows the shape and dimension of the tensile specimen with a gauge distance of 15 mm. The tests were repeated three times, and the strain rate was 10-3 s^{-1}. The macro digital image correlation (DIC) tests were performed to capture the local strain distribution during the tension. The specimen surfaces were sprayed with black and white scatter dots, and the speckle images of the specimen were collected at each deformation stage using high precision camera. Subsequently, the speckle images were processed by commercial software XTDIC to obtain the local strains at the different macroscopic strains.

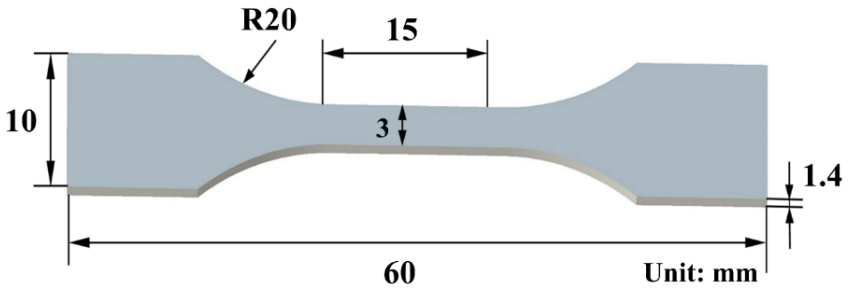

Fig. 2. Geometrical size of the uniaxial tensile specimen.

Multiscale modelling - Macroscale FE modelling. A uniaxial tensile model of the as-received steel was conducted as a macroscale finite element (FE) analysis, as showed in Fig. 3. The displacements of the plane z=0 and y=-30 mm have been constrained in the z-direction and y-direction, while the planes y=30 mm has been imposed uniform time-dependent displacement amounting to 5 mm, respectively. All other boundary surfaces of the domain have been considered traction-free. To make the simulation more accurate, the mesh size of the tensile model is divided into three sections, among which the middle segment is 0.2 mm, the circular segment is 0.5 mm, and the holding segment at both end is 1 mm. The mesh type was the eight-node linear hexahedron (C3D8R) with linear interpolation and selective reduced integration 8670 hexahedra elements, which was built via the ABAQUS/Explicit software. In addition, the Ludwik law and GTN porous plasticity model [27-29] were used as the elastic-plastic behavior and damage behavior of as-received steel, respectively. The laws are shown in following:

$$\sigma = \sigma_0 + K(\varepsilon_p)^n \tag{1}$$

$$\Phi = (\frac{\sigma_{eq}}{\sigma})^2 + 2f^* q_1 \, cosh(\frac{3q_2}{2}\frac{\sigma_m}{\sigma}) - (1 + q_3 f^{*2}) = 0 \tag{2}$$

$$f^* = \begin{cases} f, & f > f_c \\ f_c + \frac{f_u - f_c}{f_f - f_c}(f - f_c), & f_c \le f \le f_f \\ f_u, & f \ge f_f \end{cases} \tag{3}$$

$$\dot{f} = \frac{f_N}{s_N\sqrt{2\pi}} exp\left[-\frac{1}{2}\left(\frac{\bar{\varepsilon}^p_{eq} - \varepsilon_N}{s_N}\right)^2\right]\dot{\bar{\varepsilon}}^p_{eq} + (1-f)\dot{\varepsilon}^p_{eq} \tag{4}$$

where σ is the flow stress of undamaged material. σ_0 is the yield stress. K and n are the hardening modulus and exponent, respectively. σ_{eq} is the von Mises equivalent stress. σ_m is the hydrostatic pressure, which can be calculated as $\sigma_m = \frac{1}{3}\sigma_{ij}\delta_{ij}$. q_1, q_2, q_3 are the Tvergaard parameters, which are equal to 1, 1.5, and 2.25. $f_N, f_c, f_f, \varepsilon_N$ and S_N are GTN model parameters, which can be obtained by inverse extrapolation method in comparison with experimental data.

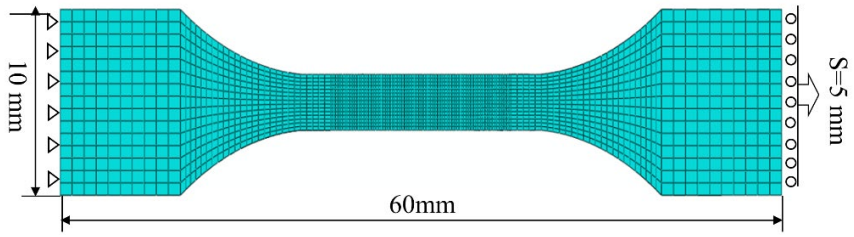

Fig. 3. The schematic of macroscale FE model: (a) tensile model; (b) zoom over the middle segment of tensile model.

Multiscale modelling - Mesoscale RVE modelling. In this section, mesoscale RVE is reconstructed based on the undeformed in-situ SEM micrographs by the image processing method [30, 31]. The generated RVE model, consisting of 456 particles, is presented in Fig. 4. The volume fraction of spheroidized cementite in the RVE was 20.12%. Subsequently, the generated RVEs were meshed in the commercial software ABAQUS (2020) with the 3-node linear plane stress triangle (CPS3) elements. The total number of elements and nodes are 151040 and 148007, respectively. To simulate the tensile deformation, symmetric boundary condition (SBC) was used by constraining all nodes of each element along the left edge in the X direction and move freely in the Y direction, and all nodes on the bottom edge to move in the Y direction but were free to move in the X direction. In addition, the cementite particles were assumed to follow linear elasticity with a Young's modulus of 230 GPa. Linear elasticity with a Young's modulus of 205 GPa and Ludwik law were used to describe the elastic-plastic behavior of ferrite matrix. According to the inverse analysis method based on genetic algorithm (GA), the model parameters for ferrite phase was obtained.

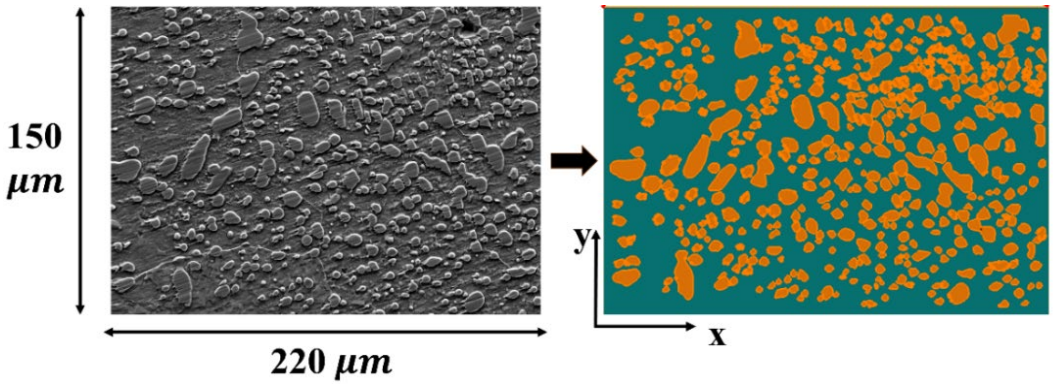

Fig. 4. A composite view of the reconfigured RVE model from the undeformed in-situ SEM image.

Multiscale modelling – Nanoscale MD modelling. To analyze the interfacial debonding between ferrite and cementite under the tension, MD simulations were conducted by using the atomic/molecular Massively Parallel Simulator (LAMMPS) package. Due to irregular morphology of cementite particles, the interface between ferrite matrix and cementite particles are subjected to mixed-mode loading [32]. The size of box is 300 Å in the x direction, 200 Å in the y direction, and 150 Å in the z direction, for a total of 848249 atoms. The orientation relationship between the ferrite and cementite was based on the transmission electron microscopy (TEM) test. Therefore, a ferrite-cementite interface model was generated using the Atomsk software, which is shown in Fig. 5.

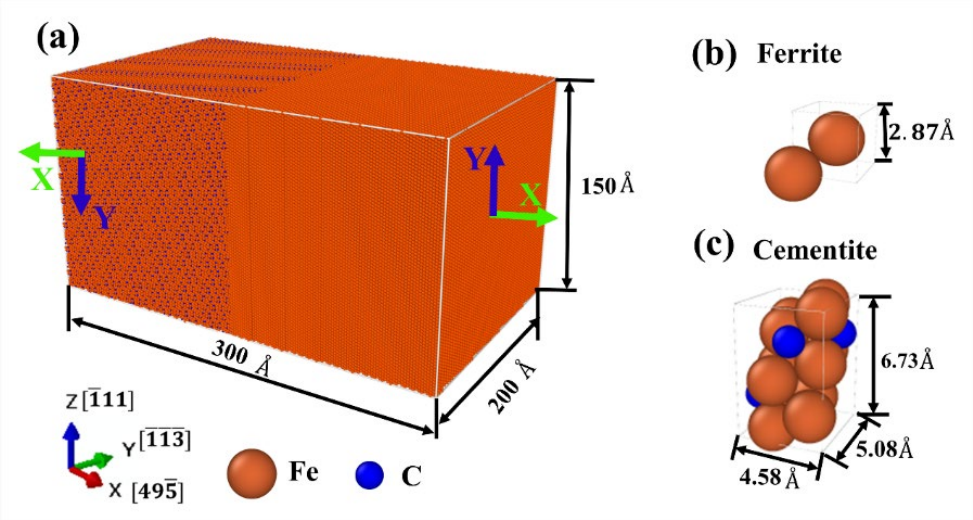

Fig. 5. A schematic of MD simulations to obtain the traction-separation (T-S) behavior at the matrix/particle interface.

Additionally, an embedded atom method (EAM) potential for Fe-C system was utilized to describe the atomic interaction, which has been verified to be reliable [33]. Before loading, the model was relaxed for 100 ps under the isothermal-isobaric (NPT) conditions to allow the system to reach most stable state. Afterwards, the relaxed model was carried out at a strain rate 10^9 s^{-1} along x and y directions (corresponded to the normal and shear directions) until fracture, respectively. The mixed mode loading conditions are determined by the shear and normal strain rate, respectively. The two strain rates are proportional to the rates of boundary displacements in the x and y directions, $\triangle \dot{X}$ and $\triangle \dot{Y}$. The relative normal and shear loading condition is expressed by a loading angle, $\theta = ArcTan(\frac{\triangle \dot{X}}{\triangle \dot{Y}})$. In order to obtain sufficient data for traction-separation relationships, MD simulations were carried out at five selected loading angles ($\theta = 0, 30°, 45°, 60°, 90°$). Finally, the stress-strain curves were obtained to represent the traction(τ)-separation (δ) behaviors.

Results and discussion

Microstructural characterization. The typical microstructure and statistical result are presented in Fig. 6. As presented in Fig. 6(a)~(b), the microstructure of as-received steel was consisted of ferrite matrix (dark zone, α) and randomly distributed cementite particles (bright zones, θ), in which the morphologies of particles were spherical. The particle volume fraction is about 20%, and the particle diameters range from 0.1~1 μm. As illustrated in Fig. 6(c)~(f), the ferrite/cementite interface is semi-coherent with a lattice misfit of 7.6%. The zone axes of ferrite and cementite were not exactly parallel, and the orientation relationship (OR) of the ferrite/cementite interface was $[\bar{1}0\bar{1}]_\alpha \parallel [\bar{2}11]_\theta$.

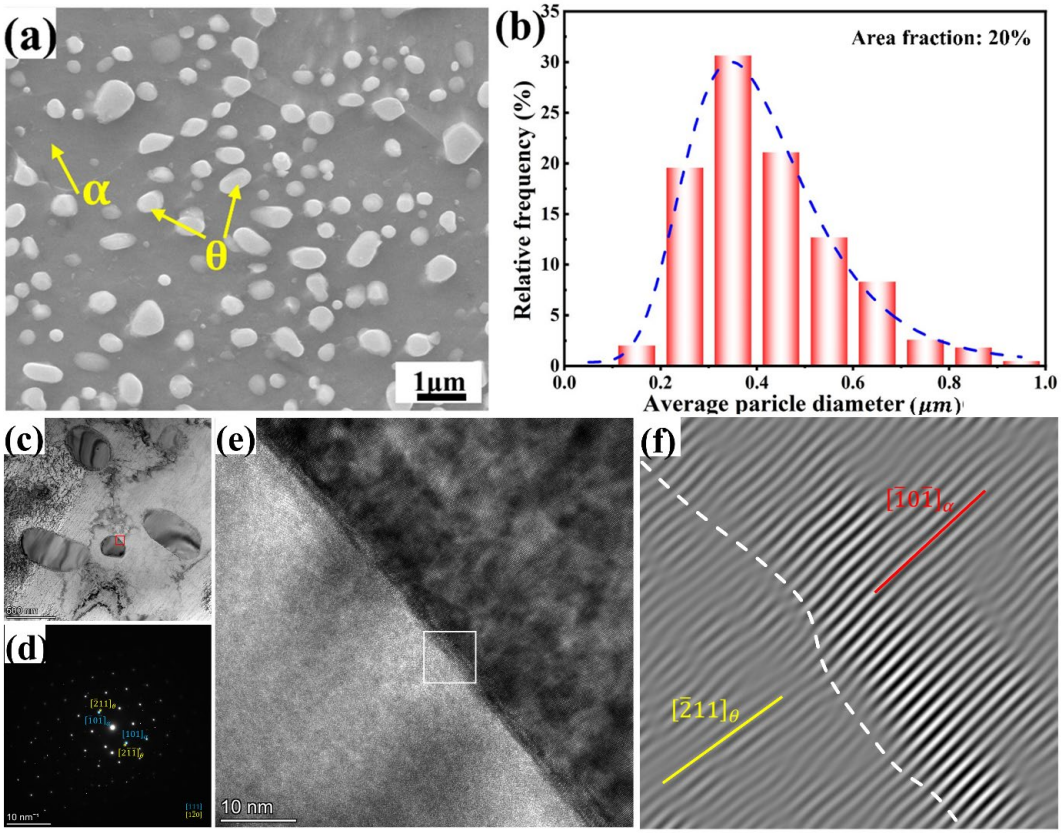

Fig. 6. Initial microstructural observations from SEM and TEM tests: (a) SEM image, (b) size distribution histogram of cementite particles. (c) Bright-field TEM image of ferrite and cementite. (d) Corresponding selected area diffraction pattern of the interface along $[001]_\alpha$ *zone axis. (e) HRTEM image of the interface observed from the red-boxed area in (c). (f) FFT image of the region labeled by the white box in (e).*

In situ SEM images, corresponding to the different global strains marked in Fig. 1(b), are shown in Fig. 7. As shown in Fig. 7, the as-received steel was consisted of the ferrite matrix and cementite particles. In the strain of 2%, no obvious variation occurred in the microstructure. When the strain was increased to 5%, several plastic slip bands appeared in the ferrite phase (marked by yellow dotted lines), and a bar-shaped cementite particle was broken (marked by red dotted box). At a strain of 10%, numerous plastic slip bands were observed in the ferrite phase, which showed a 45° angle to the direction of loading. As the strain reached to 15%, significant plastic deformation was observed in the ferrite phase. A large number of micro-voids (marked by green dotted circles) were detected at the interface between ferrite and cementite particles. Once the strain further increased to 20%, the volume fraction of voids between ferrite and cementite increased. In addition, voids in the ferrite phase were also observed (marked by pink triangle). From the above damage process, three types of damage mechanisms can be summarized: (1) Interfacial debonding; (2) cementite cracking; (3) ferrite cracking. Among them, the final fracture mainly occurred from the interface-debonding voids. In addition, the particles with irregular shapes were more likely to undergo fracture, rather than eventual failure.

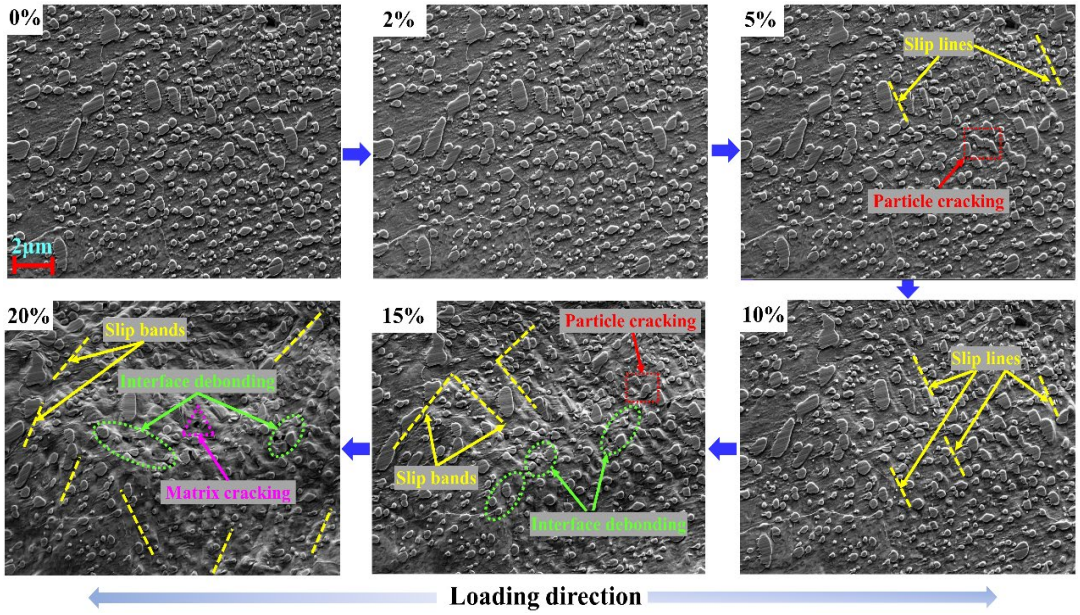

Fig. 7. SEM images at magnification of 5000×, corresponding to the strains of 0%, 2%, 5%, 10%, 15% and 20% for in situ tensile test.

Macroscale mechanical properties. Fig. 8 shows the experimental stress-strain curves and strain distributions by macro DIC analysis. As shown in Fig. 8(a), the yield stress and elongation are 407.26 MPa and 24.47%, respectively. As presented in Fig. 8(b), the strain distribution of as-received steel is extremely heterogeneous. When the engineering strain increases to the 0.15 (marked by the point A), the local strain ($\boldsymbol{\varepsilon_{xx}}$) in the central region of specimen is 0.205. As the engineering strain reaches the necking stage of the specimen (marked by the point B), the local strain ($\boldsymbol{\varepsilon_{xx}}$) in the central region increases to 0.508.

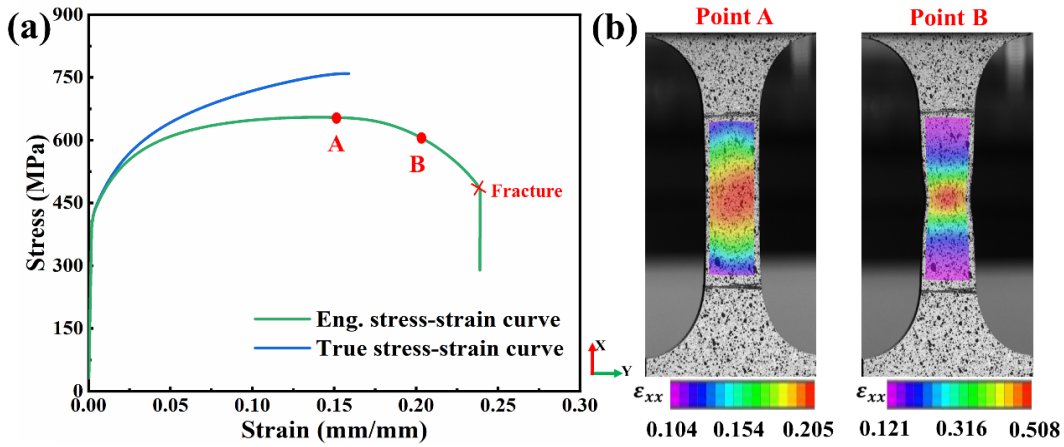

Fig. 8. (a) Stress-strain curves of uniaxial tensile experiment. (b) Strain distribution captured by macro DIC analysis.

To identify the model parameters in the macroscale FE simulation, the inverse extrapolation method was used to identify the unknown parameters in combination with experimental and simulated results under uniaxial tensile loading. First, the Young's modulus (E) was obtained by fitting the experimentally elastic stage of the true stress-strain curve. Second, the Ludwik model parameters were determined from fitting Eq. (1) to the true stress versus true plastic strains curves of the uniaxial tensile test. Third, the unknown GTN model parameters ($\varepsilon_N, f_c, f_N, f_f$) are calibrated by response surface method (RSM) [34]. Fig. 9 shows the simulated results in comparison with

experimental result. As shown in Fig. 9(a), the simulated force-displacement curve under the optimized damage parameters were also well fitted to the experimental results. As shown in Fig. 9(b), the strain distribution at the necking stage was well match to the experimental result (Fig. 8(b)). In presented in Fig. 9(c), the void volume fractions of central point at the necking stage are 0.02. The optimal model parameters for macroscale simulation are listed in Table 2.

Table 2. Identified material parameters for the macroscale tensile simulation.

Parameters	$E(GPa)$	σ_0	K	n	ε_N	f_N	f_c	f_f
Value	205	262	830	0.25	0.2	0.01	0.05	0.15

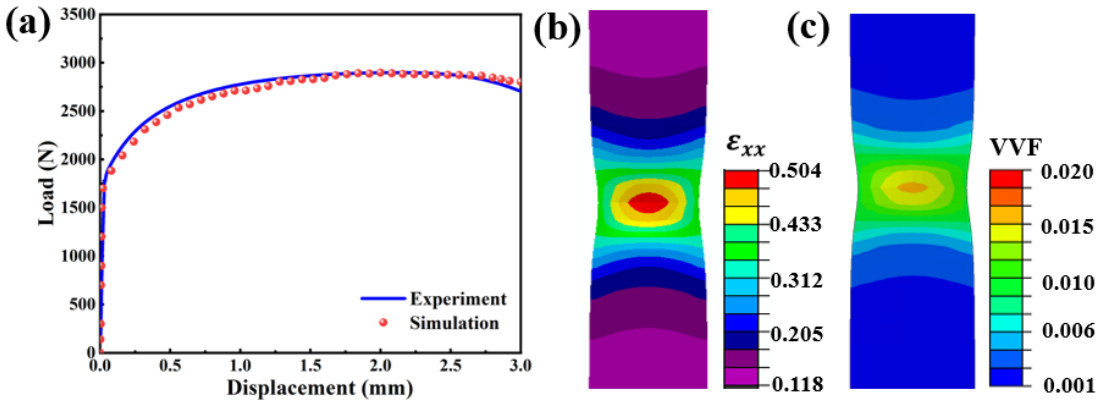

Fig. 9. (a) Stress-strain curves of uniaxial tensile test. (b) Strain distribution captured by DIC test during the tensile loading. (c)Void volume fractions of central point at the necking stage.

Mesoscale mechanical properties. Fig. 10 shows strain maps by using μDIC analysis during in situ tension. It is worth noting that strain maps could not be approached due to the excessive plastic deformation after the strain of 10%. Therefore, only the strain fields at the global strains of 2% and 5% were analyzed. In these two stages, the material damage was driven by the particle cracking. It shows that the distribution of local strains was more homogenously distributed in the ferrite matrix, while the larger strain gradients occurred close to the cementite particles. The highest localized strains were both distributed in the ferrite phase close to the irregular elongated particles. It is assumed that the particle strain in μDIC map (ε_θ^{DIC}) was equal to an average value of PEEQ of matrix surrounding to the fractured particle that was observed in in-situ SEM images. Similarly, the matrix strain (ε_α^{DIC}) was calculated by averaging the PEEQ at four surrounding points in the matrix from μ-DIC strain maps. As showed in Fig. 10(a), the local strains of ROI ranged from 0 to 0.095 at a global strain of 0.02. The averaged strain of ferrite matrix is ε_α^{DIC}= (0.048+0.035+0.008+0.064)/4=0.039 at the stage before particle fracture. In Fig. 10(b), the local strains of ROI ranged from 0.039 to 0.132 at a global strain of 0.05. The matrix strain is ε_α^{DIC}= (0.109+0.118+0.128+0.101)/4=0.114 at the stage after particle fracture.

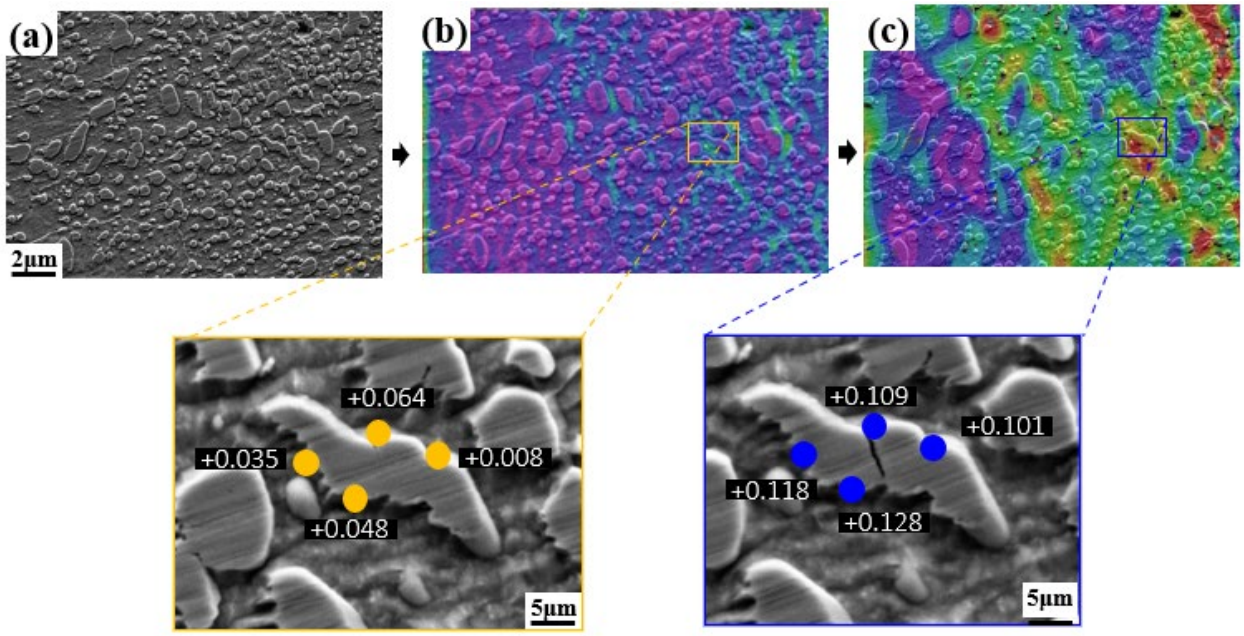

Fig. 10. Strain maps and matrix strain points by using μ-DIC technology from the in-situ tensile test with the global strain of (a) 0%, (b) 2%, (c) 5%.

Fig. 11 shows the micromechanical behaviors of as-received steel were analyzed using microstructure-based RVE simulation. It can be seen from Fig. 11(a) that the stress distribution in the ferrite phase was heterogeneous, and increased preferentially along the ferrite phase around the large particle. The stress localization became more pronounced with increasing strain, localizing along a direction 45° to the loading direction. Similarly, the stress distribution in the cementite phase exhibited the same inhomogeneity, as shown in Fig. 11(b). In addition, the stresses along the tips of the particles or in the depressed regions with a small radius of curvature were significantly higher than in other locations with higher roundness. In Fig. 11(c), the strain distribution in the ferrite and cementite phases is also inhomogeneous, and strain localization gradually develops with increasing strain. These results indicate that the mismatched properties between the cementite and ferrite led to an inhomogeneous distribution of the mesoscale stresses and strains between the two phases. The internal stresses and strains of the ferrite and cementite phases also showed inhomogeneous distributions. The inhomogeneous profiles were closely related to the shape, size, and distribution of the particles, and to the level of plastic slip of the ferrite.

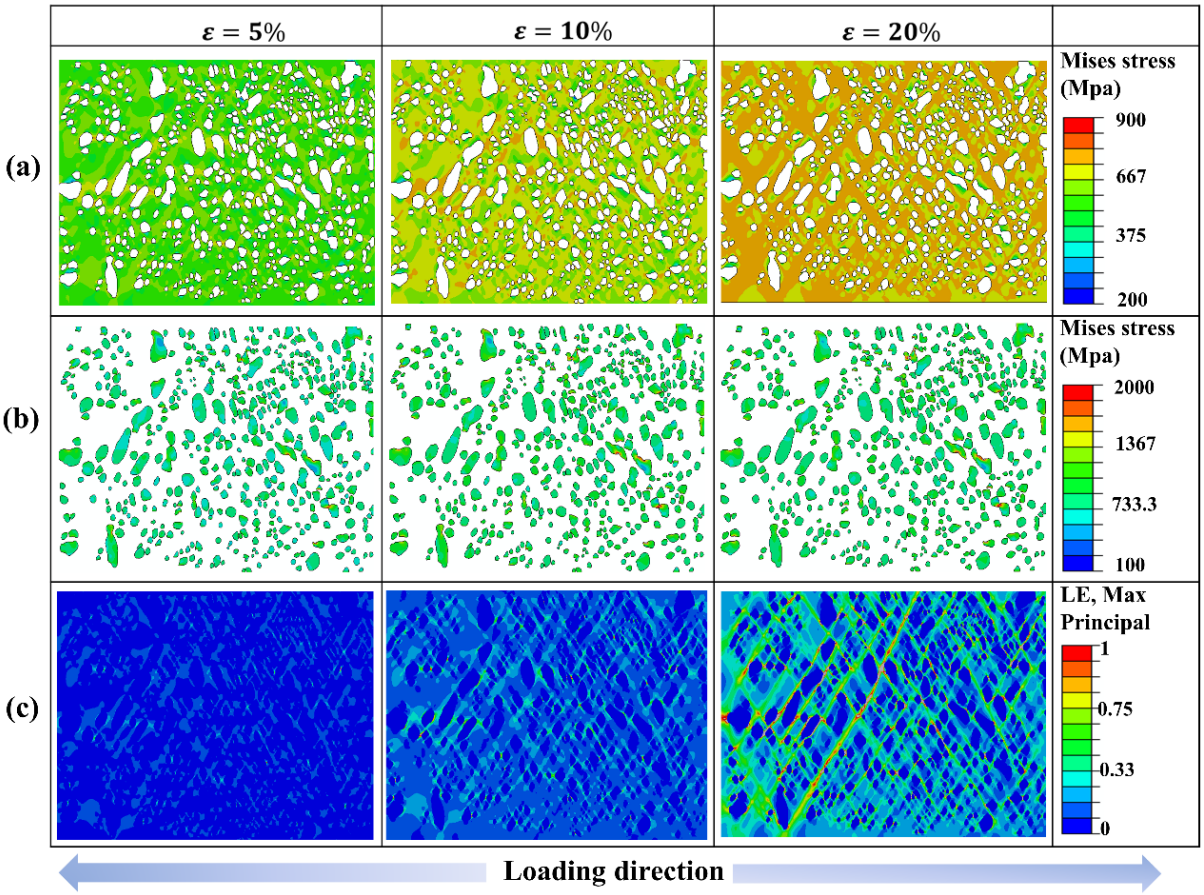

Fig. 11. The strain and stress distributions of the local microstructure under the in-situ tensile loading: (a) mises stress in ferrite phase, (b) mises stress in cementite phase, and (c) maximum principal strain.

Nanoscale MD results. Fig. 12 shows the interfacial decohesion of ferrite-cementite interface by MD simulation under the normal loading. As shown in Fig. 12(a), decohesion preferentially appears at the interface of the two phases , as well as fracture with increasing strain. In presented in Fig. 12(b), a large plastic slip occurred in the ferrite, while the cementite phase remaind essentially elastically deformed. This also indicated the interfacial debonding caused by the large strain gradient difference between the ferrite and cementite phases. As illustrated in Fig. 12(c), the maximum force and total energy to separation for interfacial debonding under different angles of loading are varied. The maximum traction of interface debonding was 3.26 GPa under pure shear loading (marked with purple line), and the corresponding failure displacement to separation was 80Å. Under uniaxial tension, the maximum stress and displacement were 7.41 GPa and 45 Å, respectively. Interfacial debonding occurred preferentially under shear loading compared to tensile loading. Conversely, complete fracture was delayed much more under shear loading than under tensile loading. Comparing the displacements for the onset of interface debonding and the displacements for the final failure under different loading, there is a gradual transfer from shear to tensile with a gradual delay.

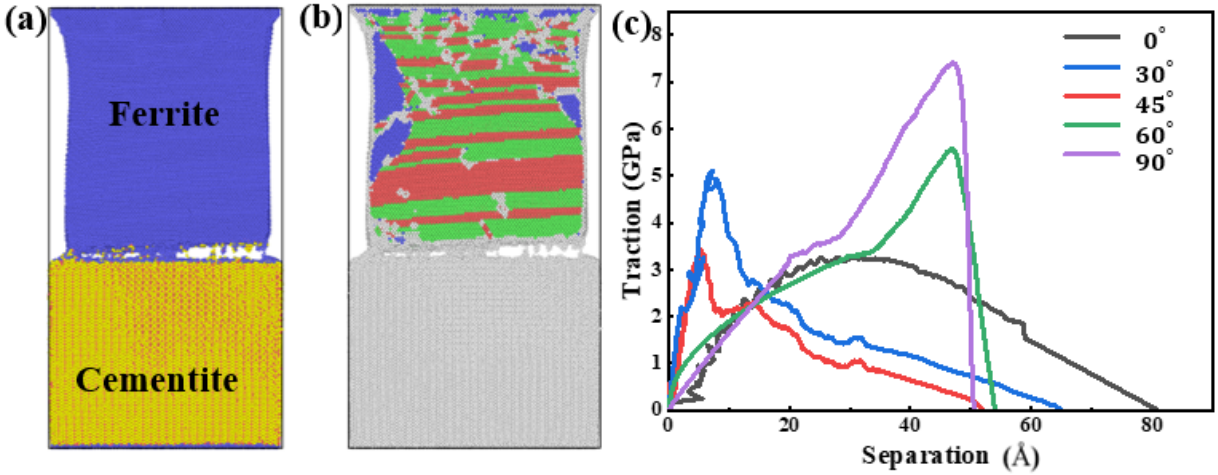

Fig. 12. Traction-separation beahvior of ferrite-cementite interface by MD simulation: (a) interfacial debonding; (b) Comoin neighbor analysis (CNA); (c) traction-separation curves under different angle loading. Noting that the CAN can be used to reflect the capacity for plastic deformation.

Summary

The damage and fracture behavior of high-carbon steel containing ferrite and cementite particles are systematically investigated through multiscale finite element simulation and in situ experiment. The experimental results demonstrated that the damage mechanism of high-carbon steel under tensile loading primarily involved strip-shaped particle cracking, interfacial debonding at the two phases, and cracking within the ferrite matrix. Moreover, it is worth noting that material fracture ultimately occurs due to interfacial debonding. The multiscale simulations indicated a large plastic deformation of the ferrite under large deformations, while the particles maintained the elastic deformation. This large strain localization led to the ultimate failure of the material, and the morphology, size and distribution of the particles strongly influence the void initiation. The driving forces for the three types of damage mechanism were equivalent stresses, maximum principal stresses, and equivalent plastic strains, respectively. In addition, interfacial debonding occurred preferentially under shear loading and is most difficult to occur under tensile loading. This work provides significant guidance for the subsequent modulation of the microstructure and forming parameters of this steel.

References

[1] T.A. Zubkova, I.L. Yakovleva, L.E. Kar Kina, I.A. Veretennikova, Study of the hardness and elastic modulus of cementite in the structure of granular pearlite by the nano-indentation method, Met. Sci. Heat Treat. 56 (2014) 330-335.https://doi.org/10.1007/s11041-014-9756-3

[2] H.J.P.i.m.S. Bhadeshia, Steels for bearings, 57 (2012) 268-435.

[3] C. Prasad, P. Bhuyan, C. Kaithwas, R. Saha, S. Mandal, Microstructure engineering by dispersing nano-spheroid cementite in ultrafine-grained ferrite and its implications on strength-ductility relationship in high carbon steel, Mater. Des. 139 (2018) 324-335. https://doi.org/10.1016/j.matdes.2017.11.019

[4] H.N. Wu, D.S. Xu, H. Wang, R. Yang, Institute, Of, Metal, Research, Chinese, Academy, Molecular Dynamics Simulation of Tensile Deformation and Fracture of γ-TiAl with and without Surface Defects, J. Mater. Res. Technol. 10 (2016) 49-58. https://doi.org/10.1016/j.jmst.2015.12.001

[5] W. Li, T. Sakai, Q. Li, L.T. Lu, P. Wang, Reliability evaluation on very high cycle fatigue property of GCr15 bearing steel, Int. J. Fatigue 32 (2010) 1096-1107. https://doi.org/10.1016/j.ijfatigue.2009.12.008

[6] M. Yang, L. Zhou, C. Wang, P. Jiang, F. Yuan, E. Ma, X. Wu, High impact toughness of CrCoNi medium-entropy alloy at liquid-helium temperature, Scr. Mater. 172 (2019) 66-71. https://doi.org/10.1016/j.scriptamat.2019.07.010

[7] Q. Deng, N.A. Bhatti, X. Yin, M. Abdel Wahab, The effect of a critical micro-void defect on fretting fatigue crack initiation in heterogeneous material using a multiscale approach, Tribol. Int. 141 (2020) 105909. https://doi.org/10.1016/j.triboint.2019.105909

[8] A. Inoue, T. Ogura, T.J.T.o.t.J.I.o.M. Masumoto, Transmission electron microscope study on deformation and fracture of cementite in cold-rolled steels, 17 (1976) 149-157.

[9] S.P. Rawal, J. Gurland, Observations on the effect of cementite particles on the fracture toughness of spheroidized carbon steels, Metall. Trans. A 8 (1977) 691-698. https://doi.org/10.1007/BF02664778

[10] K. Shibanuma, S. Aihara, K.J.E.F.M. Suzuki, Prediction model on cleavage fracture initiation in steels having ferrite–cementite microstructures–Part I: Model presentation, 151 (2016) 161-180.

[11] A. Nagao, K. Hayashi, K. Oi, S. Mitao, Effect of uniform distribution of fine cementite on hydrogen embrittlement of low carbon martensitic steel plates, ISIJ Int. 52 (2012) 213-221. https://doi.org/10.2355/isijinternational.52.213

[12] K. Shibanuma, S. Aihara, K.J.E.F.M. Suzuki, Prediction model on cleavage fracture initiation in steels having ferrite–cementite microstructures–Part II: Model validation and discussions, Eng. Fract. Mech. 151 (2016) 181-202. https://doi.org/10.1016/j.engfracmech.2015.03.049

[13] F.-F. Li, G. Fang, Stress-state dependency of ductile fracture in an extruded magnesium alloy and its underlying mechanisms, Int. J. Plast. 152 (2022) 103258. https://doi.org/10.1016/j.ijplas.2022.103258

[14] M. Brünig, S. Gerke, M. Schmidt, Damage and failure at negative stress triaxialities: Experiments, modeling and numerical simulations, Int. J. Plast. 102 (2018) 70-82. https://doi.org/10.1016/j.ijplas.2017.12.003

[15] H. Wu, X. Zhuang, Z. Zhao, Extended GTN model for predicting ductile fracture under a broad range of stress states, Int. J. Solids Struct. 239-240 (2022) 111452. https://doi.org/10.1016/j.ijsolstr.2022.111452

[16] Q. Deng, L. Xiong, Y. Chen, Coarse-graining atomistic dynamics of brittle fracture by finite element method, Int. J. Plast. 26 (2010) 1402-1414. https://doi.org/10.1016/j.ijplas.2010.04.007

[17] V.S. Krasnikov, A.E. Mayer, Plasticity driven growth of nanovoids and strength of aluminum at high rate tension: Molecular dynamics simulations and continuum modeling, Int. J. Plast. 74 (2015) 75-91. https://doi.org/10.1016/j.ijplas.2015.06.007

[18] K. Paveebunvipak, V. Uthaisangsuk, Microstructure based modeling of deformation and failure of spot-welded advanced high strength steels sheets, Mater. Des. 160(DEC.) (2018) 731-751. https://doi.org/10.1016/j.matdes.2018.09.052

[19] A. Tang, H. Liu, R. Chen, G. Liu, Q. Lai, Y. Zhong, L. Wang, J. Wang, Q. Lu, Y. Shen, Mesoscopic origin of damage nucleation in dual-phase steels, Int. J. Plast. 137 (2021) 102920. https://doi.org/10.1016/j.ijplas.2020.102920

[20] K. Ismail, A. Perlade, P.J. Jacques, T. Pardoen, L. Brassart, Impact of second phase morphology and orientation on the plastic behavior of dual-phase steels, Int. J. Plast. 118 (2019) 130-146. https://doi.org/10.1016/j.ijplas.2019.02.005

[21] U.B. Asim, M.A. Siddiq, M.E. Kartal, A CPFEM based study to understand the void growth in high strength dual-phase titanium alloy (Ti-10V-2Fe-3Al), Int. J. Plast. 122 (2019) 188-211. https://doi.org/10.1016/j.ijplas.2019.07.002

[22] H.-J. Guo, C. Ling, E.P. Busso, Z. Zhong, D.-F. Li, Crystal plasticity based investigation of micro-void evolution under multi-axial loading conditions, Int. J. Plast. 129 (2020) 102673. https://doi.org/10.1016/j.ijplas.2020.102673

[23] J. Kang, N.S. Pottore, H. Zhu, C.C. Tasan, An in situ investigation of neighborhood effects in a ferrite-containing quenching and partitioning steel: Mechanical stability, strain partitioning, and damage, Acta Mater. 254 (2023). https://doi.org/10.1016/j.actamat.2023.118985

[24] Z. Yang, J. Fan, Y. Liu, Z. Yang, Y. Kang, J. Nie, Effect of combination variation of particle and matrix on the damage evolution and mechanical properties of particle reinforced metal matrix composites, Mater. Sci. Eng. A 806 (2021). https://doi.org/10.1016/j.msea.2021.140804

[25] M. Yaghoobi, Z. Chen, A.D. Murphy-Leonard, V. Sundararaghavan, S. Daly, J.E. Allison, Deformation twinning and detwinning in extruded Mg-4Al: In-situ experiment and crystal plasticity simulation, Int. J. Plast. 155 (2022). https://doi.org/10.1016/j.ijplas.2022.103345

[26] X.H. Gong, Z.D. Feng, D. Fan, L. Lu, S.N. Luo, Strain localization in titanium investigated via in situ digital image correlation with multiscale speckles, Mater. Charact. 189 (2022). https://doi.org/10.1016/j.matchar.2022.111940

[27] Gurson, L. A, Continuum Theory of Ductile Rupture by Void Nucleation and Growth: Part I—Yield Criteria and Flow Rules for Porous Ductile Media, J. Eng. Mater. Technol. 99 (1977) 297-300. https://doi.org/10.1115/1.3443401

[28] A. Needleman, V. Tvergaard, An analysis of ductile rupture in notched bars, J. Mech. Phys. Solids 32 (1984) 461-490. https://doi.org/10.1016/0022-5096(84)90031-0

[29] V. Tvergaard, Influence of voids on shear band instabilities under plane strain conditions, Int. J. Fract. 17 (1981) 389-407. https://doi.org/10.1007/BF00036191

[30] C. Shen, C. Wang, M. Huang, N. Xu, S. van der Zwaag, W. Xu, A generic high-throughput microstructure classification and quantification method for regular SEM images of complex steel microstructures combining EBSD labeling and deep learning, J. Mater. Res. Technol. 93 (2021) 191-204. https://doi.org/10.1016/j.jmst.2021.04.009

[31] H. Wang, F. Wang, D. Qian, F. Chen, Z. Dong, L. Hua, Investigation of damage mechanisms related to microstructural features of ferrite-cementite steels via experiments and multiscale simulations, Int. J. Plast. 170 (2023). https://doi.org/10.1016/j.ijplas.2023.103745

[32] X.W. Zhou, J.A. Zimmerman, E.D. Reedy, N.R. Moody, Molecular dynamics simulation based cohesive surface representation of mixed mode fracture, Mech. Mater. 40 (2008) 832-845. https://doi.org/10.1016/j.mechmat.2008.05.001

[33] M. Guziewski, S.P. Coleman, C.R. Weinberger, Atomistic investigation into the atomic structure and energetics of the ferrite-cementite interface: The Bagaryatskii orientation, Acta Mater. 119 (2016) 184-192. https://doi.org/10.1016/j.actamat.2016.08.017

[34] X. Li, M. Xu, Z. Zhang, Hot damage evolution in a high strength aluminum alloy during hot forming: a study using the Gurson–Tvergaard–Needleman model, J. Mater. Res. Technol. 14 (2021) 1366-1376. https://doi.org/10.1016/j.jmrt.2021.07.066